Energy Technology
Generation, Conversion, Storage, Distribution
www.entechnol.de

Unraveling the Energy-Harvesting Performance of Antimony-Doped $BaTiO_3$ Toward Self-Powered on-Body Wearable Impact Sensor

*Rayavarapu Vamsi, Durgaraju Kanaka Harshitha, Kaliyannan Manojkumar, Dhara Sateesh, Rajaboina Rakesh Kumar, Jananipriya Boominathan, Sugato Hajra, Swati Panda, Hoe Joon Kim, and Venkateswaran Vivekananthan**

Harvesting ambient mechanical energy from the environment has gained immense interest due to its application in energy harvesting and active sensing. Herein, an ABO_3 class ferroelectric semiconducting material $BaTiO_3$ nanoparticles are used, and Antimony (Sb) is used as a dopant, which can be able to enhance the piezoelectric coefficient of $BaTiO_3$ to a higher level, leading to increased energy-harvesting performances. The fabricated antimony-doped barium titanate [Sb-doped $BaTiO_3$ designated as (BST)] is then blended with polydimethylsiloxane (PDMS) to prepare a composite film. Electrodes are then attached with the composite film on either side to fabricate the flexible composite piezoelectric nanogenerator (FCF-PENG) device. The fabricated FCF-PENG device generates a maximum electrical output of peak-to-peak 28 V and 1.5 μA, respectively. The device also shows a good power density of 1.6 mW m^{-2} at the load resistance of 80 MΩ. At last, a real-time impact sensor was fabricated to employ the device as the wearable impact sensor. The fabricated impact sensor detects the impact from high to low upon the human collision impact tested within the laboratory and the impact values are recorded and monitored with indicator using ESP32 microcontroller and ThingSpeak cloud. The above analysis and the real-time experiments proved that the fabricated impact sensor paves the way toward sports healthcare and rehabilitation with Internet of Things (IoT) devices soon.

1. Introduction

The exploration of various renewable energy sources and their integration into our daily lives represents a promising solution to current energy challenges.[1,2] Numerous nonconventional energy sources are available, offering diverse applications.[3] Among these, harvesting electrical energy from external mechanical energy stands out as a cutting-edge approach with widespread potential. For mechanical energy harvesting, nanogenerators such as piezoelectric,[4] triboelectric,[5,6] thermoelectric,[7,8] and pyroelectric[9] devices are predominantly utilized. So far piezoelectric nanogenerators were reported for performing various real-time applications ranging from biomechanical energy harvesting, self-powered pressure sensors, chemical sensors, humidity sensors, flexion sensors, muscular monitoring, gait monitoring, e-skins, and IoT-based systems.[10,11] Among the different types of nanogenerators, piezoelectric nanogenerators (PENGs) offer significant advantages, including self-powered capability, high durability, and mechanical stability.[12–18] Achieving high electrical output depends critically on the selection of appropriate piezoelectric materials. Certain materials with perovskite structures, such as lead

R. Vamsi, D. Kanaka Harshitha, K. Manojkumar, D. Sateesh, V. Vivekananthan
Centre for Flexible Electronics, Department of Electronics & Communication Engineering
Koneru Lakshmaiah Educational Foundation
522302 Guntur, Andhra Pradesh, India
E-mail: vivek@kluniversity.in

V. Vivekananthan
Department of Integrated Research & Discovery, Department of Electronics & Communication Engineering
Koneru Lakshmaiah Educational Foundation
522302 Guntur, Andhra Pradesh, India

The ORCID identification number(s) for the author(s) of this article can be found under https://doi.org/10.1002/ente.202500047.

DOI: 10.1002/ente.202500047

R. R. Kumar
Energy Materials and Devices (EMD) Lab, Department of Physics
National Institute of Technology Warangal
506004 Warangal, Telangana, India

J. Boominathan
Department of Data Science
PSCMR College of Engineering and Technology
520001 Vijayawada, Andhra Pradesh, India

S. Hajra, S. Panda, H. J. Kim
Department of Robotics and Mechatronics Engineering
Daegu Gyeongbuk Institute of Science and Technology
Daegu 42988, Republic of Korea

zirconate titanate (PZT) and lead magnesium niobate-lead titanate (PMN-PT), exhibit high piezoelectric coefficients.[19,20] However, their major drawback lies in their lead content, which poses severe risks to human health and the environment. With rapid advancements in wearable electronics, there is an increasing demand for self-powered sensors operating at nanoscale dimensions.[21] These sensors must combine high stability, sensitivity, and feasibility for nanoscale fabrication. Addressing this challenge involves developing wearable impact monitoring systems that can enhance patient care through real-time impact detection.[22]

Among various lead-free piezoelectric materials such as potassium sodium niobate ($KNaNbO_3$), barium titanate ($BaTiO_3$), zinc oxide, and bismuth titanate ($BiTiO_3$), $BaTiO_3$ emerges as a promising alternative to lead-based piezoelectric materials due to its simple fabrication process and a better piezoelectric coefficient of around ≈120 pC/N, which can be comparable to PZT. However, the piezoelectric coefficient of pure BTO is relatively lower than most of the lead-based piezoelectric materials, resulting in limited electrical output. Enhancing the piezoelectric properties of BTO is achievable through appropriate doping.[23] The resulting flexible composite film-based piezoelectric nanogenerator (FCF-PENG) exhibits superior mechanical flexibility and enhanced energy-harvesting capabilities.[24–30] The FCF-PENG is further optimized to operate as a wearable energy-harvesting device, with real-time applications demonstrated in sports and healthcare environments.[31] The ability of these devices to dynamically monitor mechanical impacts and transmit data wirelessly showcases their potential for seamless integration into the Internet of Things (IoT)-enabled systems[32–37] paving the way for advanced human–machine interfaces and smart sensor technologies.[38–41]

In this work, we synthesized Sb-doped BTO nanoparticles (designated as BST nanoparticles) using a solid-state reaction method and characterized structurally using sophisticated characterization techniques. Antimony has been doped into BTO at various percentages without disturbing the tetragonal structure of the BTO. The synthesized BST nanoparticles were blended with the polydimethylsiloxane (PDMS) matrix to fabricate the BST/PDMS composite films. The fabricated composite films were made into the required dimensions attached with electrodes on either side, and packed with PDMS to fabricate the required FCF-PENG device. The device demonstrated exceptional mechanical flexibility, durability, and enhanced energy harvesting performance, with the $x = 0.07\%$ Sb-doped BST composition exhibiting the highest output among the samples. The fabricated FCF-PENG device is capable of charging commercial capacitors and additionally, FCF-PENG device was made into an on-body wearable chest band with three devices placed to detect the collision impact during sports and athletic activities. The FCF-PENG is then integrated into an IoT-enabled system using microcontrollers that is capable of real-time data acquisition, cloud-based monitoring, and mobile alert generation.

2. Materials and Characterization

2.1. Synthesis of BST Nanoparticles

BST nanoparticles were synthesized via the solid-state reaction (SSR) method. High-purity precursors, barium carbonate ($BaCO_3$, 99.5%), titanium dioxide (TiO_2, 99.99%), and antimony pentoxide (Sb_2O_5, 95%), were purchased from Merck and utilized without further modification. Precursors were thoroughly mixed using a mortar and pestle by using ethanol as a solvent to ensure uniform blending. The resulting mixture was dried in a hot air oven at 80 °C for 20 min, yielding a homogeneous dry powder. Composite was subjected to preliminary calcination in a muffle furnace at 800 °C for 3 h to initiate the reaction between the precursors and eliminate any residual volatile impurities. Subsequently, composite was ground again to ensure uniformity and heat treatment at 1100 °C for 4 h shown in **Figure 1**a–c. This high-temperature treatment promoted enhanced densification to form highly crystalline phase.[42,43]

2.2. Fabrication of PDMS/BST Composite Film

PDMS monomer and cross-linker were mixed (10:1 ratio) under magnetic stirring for 20 min to achieve a homogenous solution. To this mixture, BST was added at a constant concentration of 7 wt%, and varying proportions of the PDMS mixture at 5, 10, 15, and 20 wt% were individually prepared and stirred further for another 20 min. Resulting mixtures were poured into 100 μm thickness molds and cured at 70 °C by using a hot air oven for 2 h and yields to flexible composite films. Cured films were cut into 3 × 3 cm and attached with aluminum (Al) electrodes to establish electrical connections, and copper (Cu) wires were attached to the electrodes to charge transfer. A thin PDMS layer was attached to protect the device. Finally, the devices were electrically poled at 5 kV for 12 h prior to performing electrical analyses.[44–46]

2.3. Materials and Electrical Characterization

The crystallographic structure of the synthesized BST materials was analyzed using the X-ray diffractometer (ACS, D2 Phaser, Bruker, with Cu-Kα 1.5406 A°) and Raman spectroscopy (Renishaw Raman, Nd:YAG-532 nm monochromatic diode-pumped solid-state laser source). Surface Morphology of the material was analyzed using Scanning electron microscope (SEM, M/S SU-8230, Hitachi, Japan). The electrical response of the device was measured using an electrometer (Keithley 6514) and the vertical compressive force is applied using a linear motor (LinMot Inc., USA).

3. Result and Discussion

BST nanomaterials were prepared using solid-state reaction technique in which the precursor materials were calcined at 1100 °C to obtain the required product. The schematic diagram of the synthesis process is shown in Figure 1a–c and the detailed synthesis process is explained in the materials and characterization section. Figure 1d presents the X-ray diffraction (XRD) patterns of BST nanoparticles at varying Sb doping concentrations of 3, 5, 7, and 10%. The diffraction peaks correspond to a tetragonal perovskite structure, consistent with reference pattern (ICSD. No 96-154-2190). Prominent diffraction planes, including (100), (101), (110), (111), (200), and (211), confirm the crystallinity and phase purity of the synthesized nanoparticles. Notably,

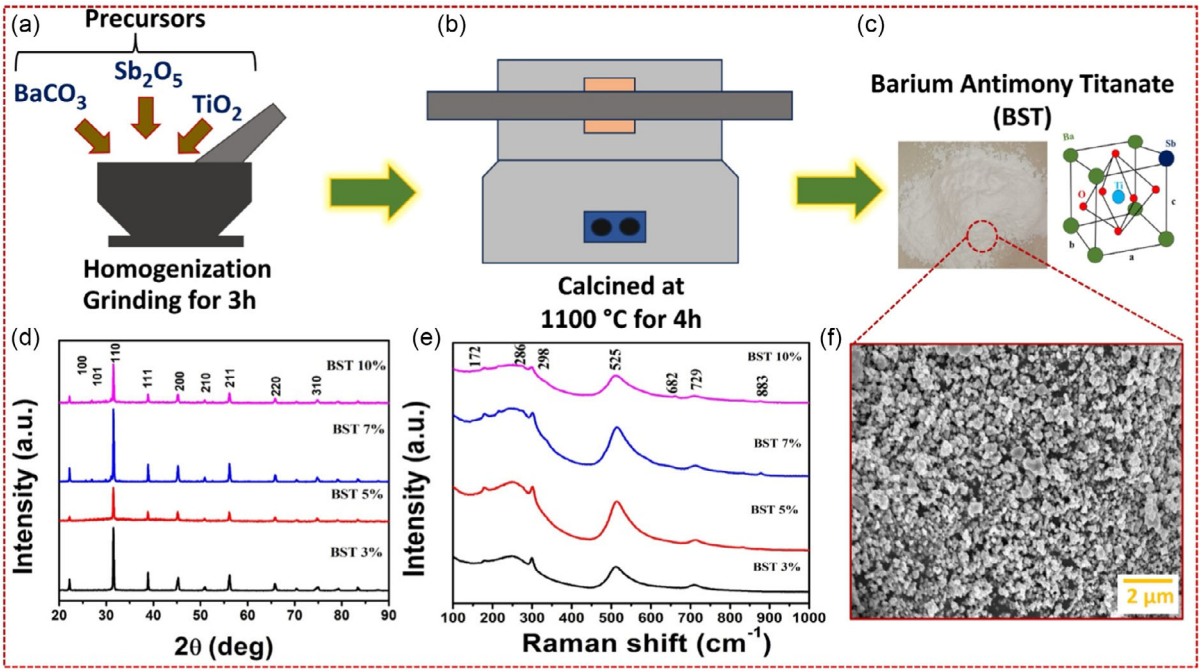

Figure 1. Synthesis of Sb-doped BTO nanoparticles and characterization. a–c) Step-by-step synthesis process of Sb-doped BTO nanoparticles using solid-state reaction technique. d) X-ray diffraction analysis of Sb-doped BTO nanoparticles with the Sb doping ratio of 3, 5, 7, and 10%. e) Raman spectroscopy analysis of Sb-doped BTO nanoparticles with the Sb doping ratio of 3, 5, 7, and 10%. f) FE-SEM analysis of the synthesized Sb-doped BTO nanoparticles with the Sb doping of 7%.

the 7% Sb-doped BTO sample exhibits the sharpest and most intense peaks, indicating superior crystallinity and reduced lattice defects compared to the other doping concentrations. This observation confirms the successful substitution of Sb ions into the BTO structure without the formation of secondary phases.[47,48] Figure 1e illustrates the Raman spectra of Sb-doped barium titanate nanoparticles with Sb doping concentrations of 3, 5, 7, and 10%. The spectra exhibit characteristic peaks associated with the vibrational modes of the tetragonal perovskite structure. Prominent peaks are observed at 172, 286, 298, 525, 682, 729, and 883 cm^{-1}, corresponding to lattice vibrations involving Ba, Ti, and O ions. Among the samples, the 7% Sb-doped BTO shows the most intense and well-defined Raman peaks, indicating enhanced structural stability and reduced lattice distortions. The intensity variations and slight shifts in peak positions across the doping concentrations suggest the successful incorporation of Sb ions into the BTO lattice, inducing localized structural modifications. Notably, the increased intensity of the 525 cm^{-1} peak in the 7% sample highlights stronger coupling of Ti–O vibrations, which is crucial for optimizing the functional properties of the material. The systematic trends observed in the Raman spectra with varying Sb doping concentrations confirm the effective tuning of lattice dynamics. The 7% Sb doping concentration demonstrates the optimal balance of structural and vibrational characteristics, making it a promising candidate for improved material performance.[47,49]

Figure 2 presents the SEM micrographs, elemental mapping, and EDS spectra of in Figure 2a pure BTO and Figure 2b BST nanoparticles, with a scale bar of 2 µm. The pure BTO sample exhibits an agglomerated, irregular granular morphology, suggesting polycrystalline nature with significant grain boundaries. In contrast, the Sb-doped BTO shows a relatively uniform particle distribution, indicating improved crystallinity and reduced agglomeration. Elemental mapping confirms the presence of Ba, Ti, and O in both samples, while Sb is distinctly observed in the doped sample. The EDS spectra further quantify elemental composition, showing Ba (38%), Ti (32%), and O (30%) in pure BTO, whereas Sb-BTO exhibits Sb (5%), Ba (35%), Ti (30%), and O (30%). The enhanced crystallinity and modified morphology in Sb-BTO suggest improved structural integrity, this piezoelectric property enables more accuracy PENG sensor applications. **Figure 3**a–c illustrates the step-by-step fabrication process of PDMS/BST composite films. The process begins with the incorporation of BST nanoparticles into a PDMS matrix, ensuring a homogeneous dispersion of the nanoparticles within the polymer (Figure 3a). Figure 3b shows the blended mixture is poured into a Petri dish and subjected to curing at 60 °C for 2 h while curing polymers undergo cross-linking and results in a flexible and robust composite film. Cured composite is carefully peeled off the mold to obtain a free-standing PDMS/BST film acts as the core active layer in the FCF-PENG device (Figure 3c). Figure 3d highlights the mechanical flexibility of the fabricated PDMS/BST composite films, shown in digital photographic images of a 3 × 3 cm film demonstrates remarkable rollable, bendable, stretchable, and twistable properties, showcasing its ability to employ various wearable and flexible electronic applications.[50,51]

Figure 3e displays a digital photographic image of the FCF-PENG, incorporating the PDMS/BST composite film. The proposed configuration ensures effective charge collection

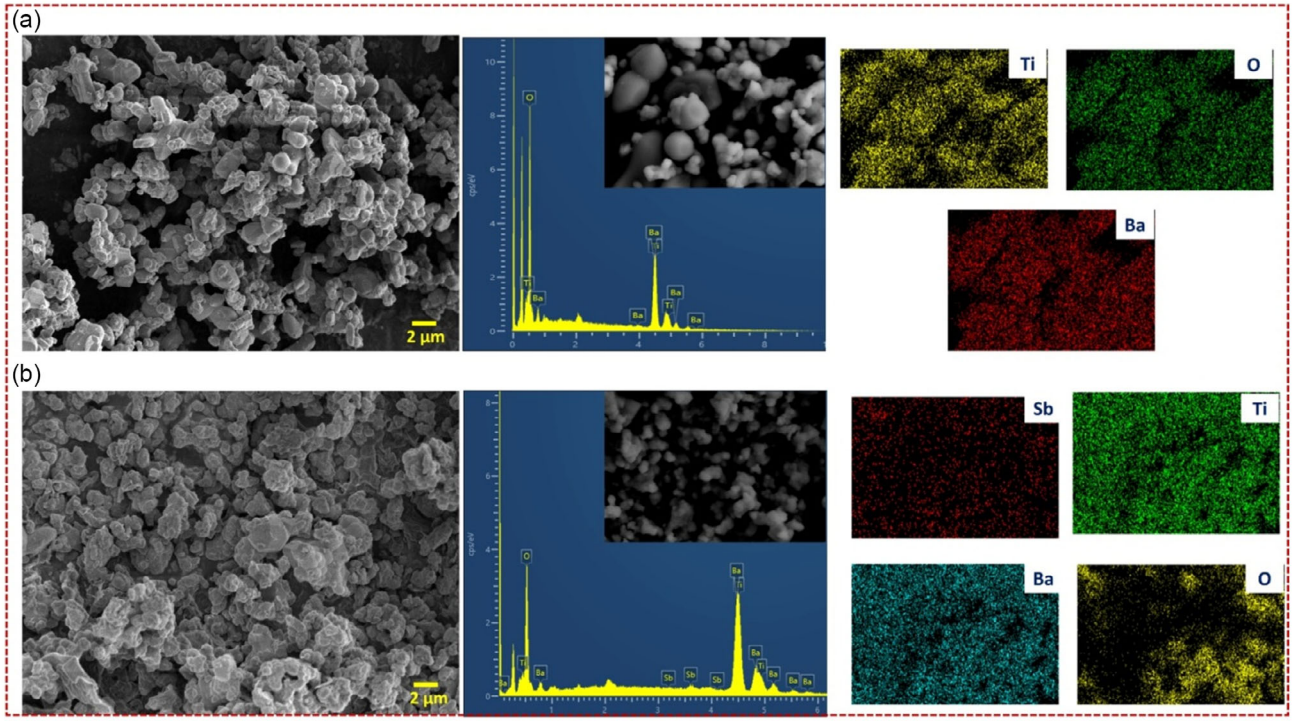

Figure 2. SEM micrographs, elemental mapping, and EDS spectra of a) pure BTO and b) antimony-doped $BaTiO_3$.

while preserving the device's mechanical robustness. Figure 3f presents a schematic representation of the sandwich layer-by-layer architecture of the flexible composite FCF-PENG device. The structure includes a dual PDMS packing layer for enhanced structural stability, a core PDMS/BST composite film act as the piezoelectric active layer, and Al electrodes for efficient charge collection. The working mechanism of Sb-Doped $BaTiO_3$ PENG for energy harvesting is illustrated in Figure 3g. The energy-harvesting mechanism of Sb-doped $BaTiO_3$ PENGs operates through four distinct stages. (i) Initial State In the absence of external stress, the material retains its perovskite structure with symmetrically aligned dipoles. Sb^{3+} doping induces localized lattice distortions, enhancing charge carrier mobility while maintaining overall charge neutrality with no electrical output. (ii) Compression mechanical pressure applied the crystal lattice deforms, causing a displacement of Ba^{2+}, Ti^{4+}, O^{2-}, and Sb^{3+} ions. This realignment of dipoles generates an internal piezoelectric field, leading to charge redistribution and electron flow through an external circuit, resulting in energy generation. (iii) Release mechanical pressure removed the lattice structure begins to recover, reversing the dipole alignment. This induces electron flow in the opposite direction, producing an alternating electrical signal. Sb^{3+} doping enhances structural stability and reduces domain pinning, facilitating efficient charge recovery. (i) Equilibrium state once the force is fully removed, the lattice returns to equilibrium, with dipoles reverting to their initial alignment. The system remains in a charge-neutral state until the next mechanical excitation restarts the process. This cyclic charge redistribution enables Sb-doped BTO PENGs to effectively convert mechanical energy into electrical power, making them promising for self-powered electronics and sensing applications.[52]

Figure 4a presents voltage versus time of the FCF-PENG device for varying Sb doping concentrations of 3, 5, 7, and 10%. Among these, the device with 7% Sb doping in BST exhibits the highest voltage output of 28 V, highlighting superior charge separation and optimal piezoelectric performance at this concentration. At 3% Sb doping, the voltage output is relatively low, peaking at ≈15 V, indicating limited charge separation. With 5% Sb doping, the voltage output improves significantly, reaching peaks around 24 V, demonstrating enhanced charge separation compared to the 3% sample. The 7% Sb-doped device achieves the highest voltage output, with peaks approaching 28 V, indicating the most efficient charge separation and piezoelectric performance. However, at 10% Sb doping, the voltage output decreases to peaks around 10 V, suggesting that excessive doping hinders effective charge separation, likely due to over-doping effects. Figure 4b illustrates the current output versus time for the FCF-PENG device with Sb doping concentrations of 3, 5, 7, and 10%. The current output trends align closely with the voltage performance for each doping level. At 3% Sb doping, the current output is the lowest, peaking at ≈0.6 μA, corresponding to its limited charge separation and low voltage performance. With 5% Sb doping, the current output increases slightly, peaking at around 0.8 μA, indicating an improvement in charge transfer efficiency. The 7% Sb-doped BST sample achieves the highest current output, peaking at ≈1.5 μA, consistent with its superior voltage output and effective charge transfer. At 10% Sb doping, the current output decreases to around 0.4 μA, reflecting reduced charge transfer efficiency, likely due to the adverse effects of

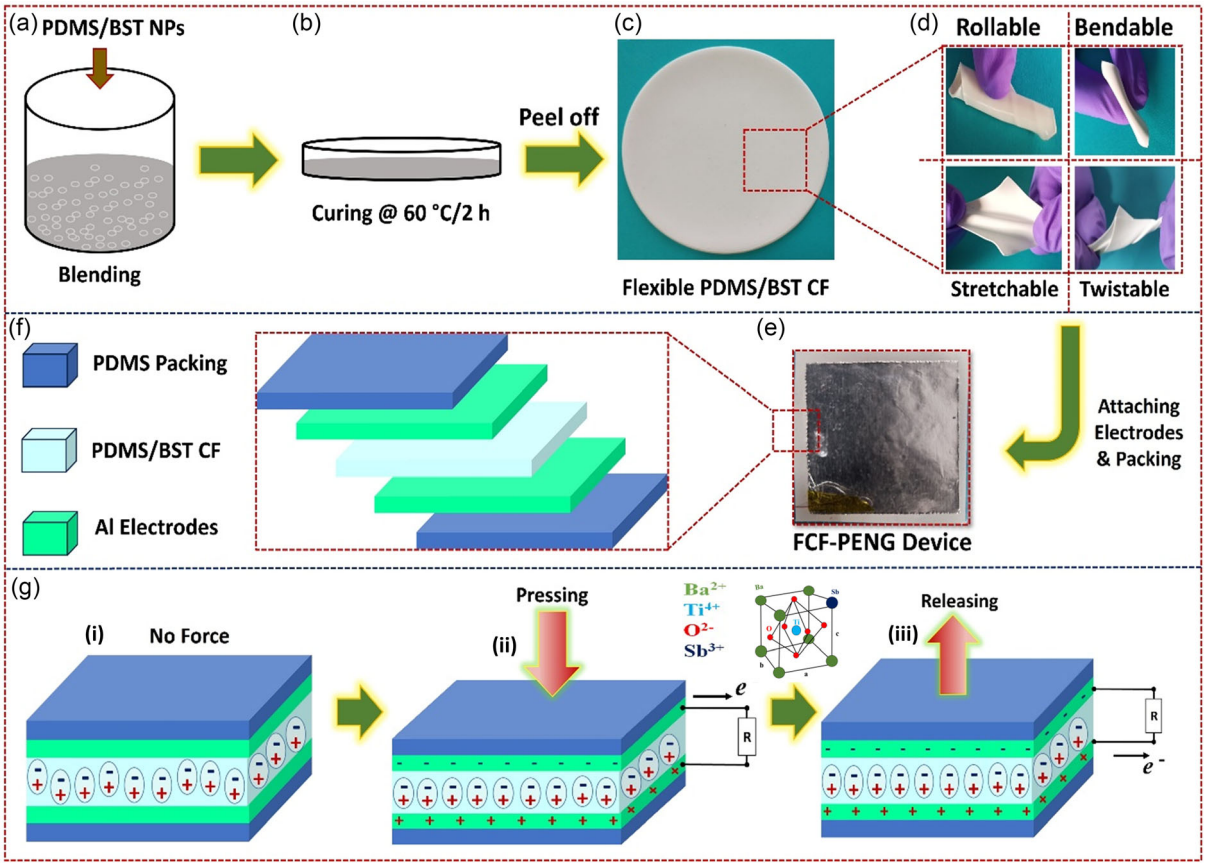

Figure 3. Preparation of PDMS/BST Nanocomposites, device fabrication and working mechanism. a–c) Step-by-step fabrication of PDMS/BST composite films. d) Digital photographic images of composite film cut at 3 × 3 cm dimension showing its rollable, bendable, stretchable and twistable nature. e) Digital photographic image of the FCF-PENG. f) Layer-by-layer schematic of the FCF-PENG device. g) Step-by-step working mechanism of FCF-PENG device.

over-doping. These results confirm that the 7% Sb doping concentration is optimal for maximizing current generation and overall device performance. Figure 4c depicts the power output of the FCF-PENG device as a function of load resistance. The power curve exhibits a distinct peak, corresponding to the impedance matching condition, where a power transfer of 1.6 μW is achieved. This highlights the importance of optimizing the external load resistance in designed circuits to maximize energy-harvesting efficiency from the device. Figure 4d provides a dual-axis analysis, showing the voltage output and power density as functions of load resistance. The voltage output increases steadily, reaching 1.7 V at higher load resistances, which aligns with the inherent characteristics of piezoelectric nanogenerators. Concurrently, the power density curve demonstrates a peak value of 1.8 mW m^{-2} at the optimal load resistance, representing the maximum energy-harvesting capability per unit area. These results emphasize the importance of impedance matching and load optimization for achieving peak performance in energy-harvesting applications. Figure 4e evaluates the capacitor charging performance of the FCF-PENG device using commercial capacitors with capacitance values of 0.1, 0.3, and 1 μF. The voltage build-up across the capacitors is plotted against time, showcasing the device's ability to effectively charge capacitors. The 0.1 μF capacitor charges more rapidly but stores less energy due to its lower capacitance, while the 1 μF capacitor takes longer to charge but can store a higher amount of energy, making it suitable for applications requiring extended power supply. The inset provides a detailed view of the dynamic charging behavior under "Force ON" and "Force OFF" conditions. During the "Force ON" state, the application of mechanical force generates electrical energy, resulting in a rapid increase in capacitor voltage. In the "Force OFF" state, the absence of mechanical force causes the voltage to stabilize or decrease gradually, reflecting the inherent self-discharge characteristics of the capacitor. This analysis highlights the capability of the FCF-PENG device to drive capacitive energy storage efficiently under dynamic operational conditions.

The real-time application and performance of the on-body wearable impact sensor system are thoroughly illustrated in **Figure 5**. The FCF-PENG device functions as a self-powered impact sensor, seamlessly integrated into wearable clothing to detect and transmit impact data in real-time. This system effectively converts mechanical forces into electrical signals, enabling dynamic monitoring. In Figure 5a, the wearable impact sensor system consists of multiple PENG units integrated into a single strip, which is wrapped around the chest. Three independent sensing units (D1, D2, and D3) are distributed along the strip,

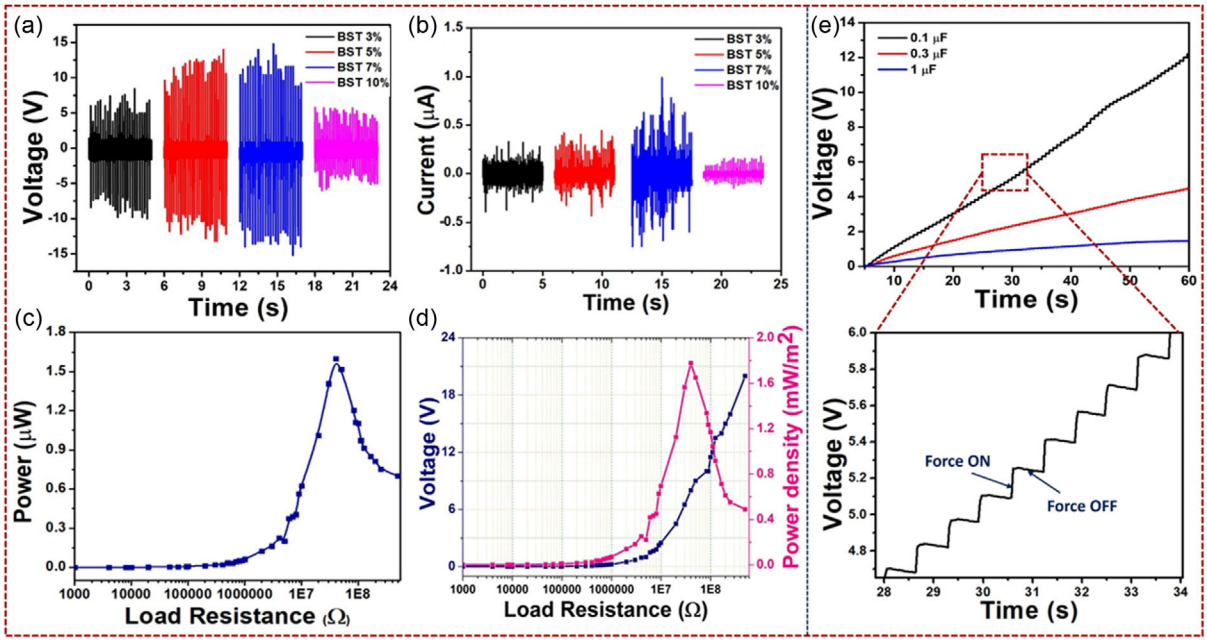

Figure 4. Electrical response analysis of FCF-PENG device. a,b) Voltage and Current output response of FCF-PENG device fabricated with Sb-doped NPs with Sb doping ratio of 3, 5, 7, and 10%. c,d) Impedance matching analysis of FCF-PENG device with which the power and power density has been analyzed. e) Charging commercial capacitors of rating 0.1, 0.3, and 1 μF, respectively, with which the inset shows the charging characteristics upon force on and force off conditions.

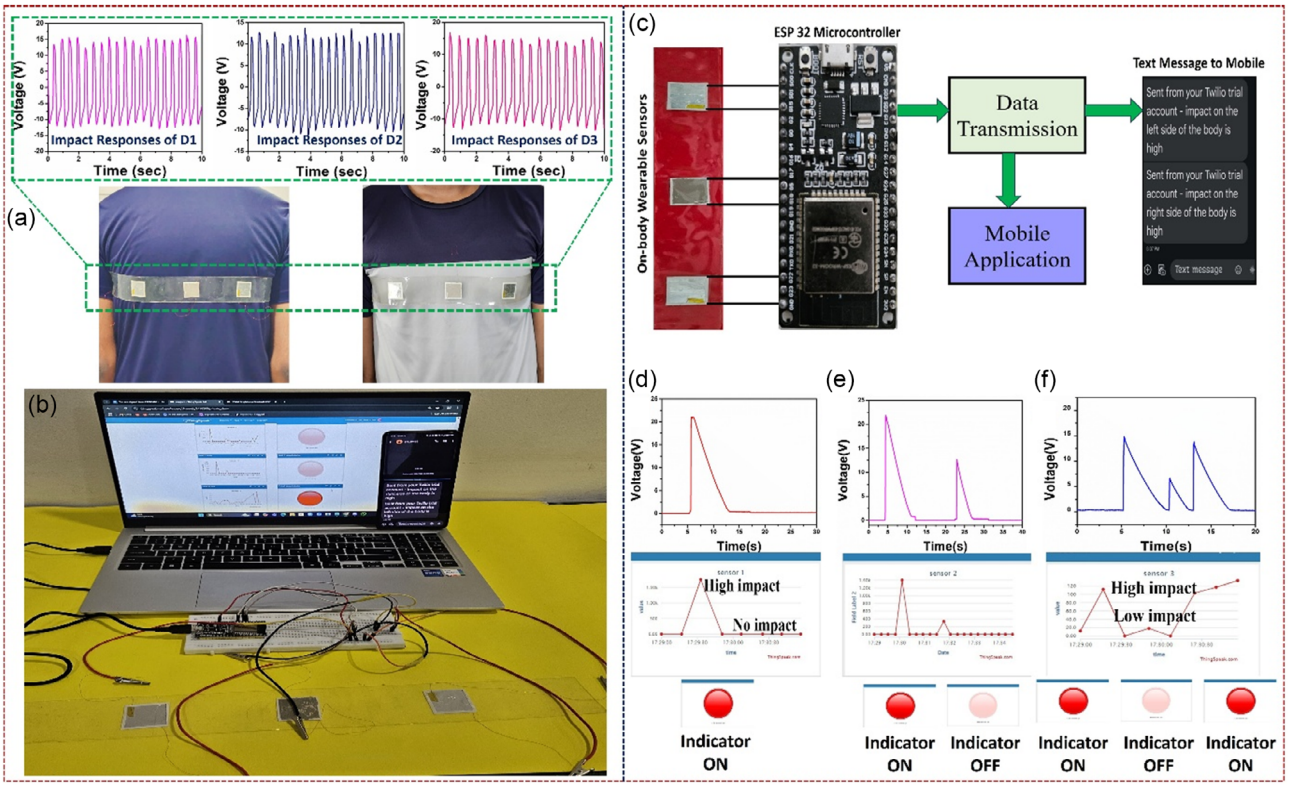

Figure 5. Real-time application of on-body wearable impact sensor. a) Digital photographic image of the fabricated impact sensor device in which the response of the individual device is given above. b) Real-time application demonstration of self-powered impact sensor using ThingSpeak cloud. c) Block diagram of the demonstrated impact sensor using ESP32 microcontroller. d–f) Impact response from the sensor and the corresponding indication on screen with indicator ON and OFF upon high-impact hit, which is the threshold.

each operating separately to capture impact data from its respective location. The inset graphs above the images illustrate the voltage responses of these individual sensors to varying mechanical impacts over time. Each sensor exhibits distinct output characteristics: D1 records high-intensity impacts, producing sharp voltage peaks; D2 responds to moderate impacts with intermediate voltage outputs; and D3 captures low-intensity forces with smaller peaks. This differentiation highlights the sensor's capability to accurately detect and quantify the intensity of localized impacts. The sensitivity and precision of the FCF-PENG-based sensor system make it invaluable for real-world applications, such as monitoring impact forces in sports to enhance athletic performance or detecting injuries in wearable healthcare systems. Figure 5b illustrates the real-time experimental setup, demonstrating the FCF-PENG device's capability to stream impact data to the ThingSpeak cloud platform. The setup consists of the wearable sensor integrated into clothing, an ESP32 microcontroller for data acquisition, and a laptop interface for live visualization of the impact data. This configuration highlights the practicality of incorporating the sensor into IoT-based systems for remote monitoring. By enabling cloud-based data storage and processing, the system provides a scalable and versatile solution for real-time impact detection in diverse applications. A schematic diagram in Figure 5c outlines the data flow and mobile alert mechanism of the sensor system. The ESP32 microcontroller processes the voltage signals generated by the piezoelectric sensors and wirelessly transmits the data to a connected mobile application. When an impact exceeding a predefined threshold is detected, the system generates a text alert and sends it to the user's mobile device. The alert specifies the location and intensity of the force, ensuring timely and actionable feedback. This integration of wearable sensors with IoT-enabled alert systems demonstrates the potential for enhanced safety, monitoring, and user interaction in real-world applications. Figure 5d–f illustrate the voltage response of the sensor to varying impact intensities, emphasizing its effectiveness in detecting and distinguishing different force levels. Under high-impact conditions, the sensor produces sharp voltage spikes that exceed the predefined threshold, triggering the on-screen indicator to switch ON and signaling a critical event that requires immediate attention. Conversely, low-impact or no-impact scenarios result in minimal voltage outputs, keeping the indicator in the OFF state, thereby filtering out non-critical forces effectively. In mixed scenarios involving both high- and low-intensity impacts, the sensor demonstrates its precision by accurately toggling the indicator ON or OFF based on whether the applied force surpasses the threshold. This capability highlights the robustness and reliability of the system in differentiating relevant events while minimizing false positives. Such performance ensures efficient and accurate monitoring in real-world applications, making the sensor system well-suited for safety-critical environments, wearable health monitoring, and athletic performance analysis.

4. Conclusion

In this study, BST nanoparticles were successfully synthesized via the solid-state reaction method, with structural and morphological analyses confirming phase purity and crystallinity. The optimized composition, containing 7% Sb doping, exhibited the highest piezoelectric performance, generating a peak output voltage of 28 V and a current of 1.5 μA. The fabricated PDMS/BST composite film demonstrated excellent mechanical flexibility and durability, making it well-suited for wearable applications. The resulting FCF-PENG device functioned as an efficient, self-powered impact sensor, seamlessly integrating with an IoT-enabled system for real-time data acquisition and wireless monitoring. Achieving a maximum power density of 1.8 mW m^{-2}, the device successfully captured and transmitted mechanical impact data, highlighting its potential for next-generation energy harvesting and smart sensing applications. These findings underscore the promise of BST-based PENGs in the development of advanced wearable electronics, impact monitoring systems, and sustainable energy solutions.

Acknowledgements

The authors thank Department of Science and Technology, Government of India for the support through PURSE program (SR/PURSE/2023/196). The work is also supported by the National Research Foundation of Korea (NRF), funded by the Ministry of Science and ICT of Korea (RS-2024-00346135 and RS-2024-00406674).

Conflict of Interest

The authors declare no conflict of interest.

Data Availability Statement

Research data are not shared.

Keywords

energy harvesting, nanomaterials, piezoelectric nanogenerators, self-powered sensor, wearable impact sensor

Received: January 8, 2025
Revised: February 15, 2025
Published online:

[1] X. Yin, H. Fu, B. Xu, *Adv. Energy Mater.* **2024**, *14*, 2304355.
[2] H. Sheng, Y. Ma, H. Zhang, J. Yuan, F. Li, W. Li, E. Xie, W. Lan, *Adv. Mater. Technol.* **2024**, *9*, 2301796.
[3] R. Singh, B. B. Krishna, J. Kumar, T. Bhaskar, *Bioresour. Technol.* **2016**, *199*, 398.
[4] L. Zhang, J. Kan, S. Lin, W. Liao, J. Yang, P. Liu, S. Wang, Z. Zhang, *Renewable Energy* **2024**, *222*, 119796.
[5] X. Gong, H. Zhang, X. Li, *J. Alloys Compd.* **2024**, *976*, 173230.
[6] P. K. Nitha, A. Chandrasekhar, *ACS Appl. Electron. Mater.* **2024**, *6*, 5314.
[7] Y. Yang, K. C. Pradel, Q. Jing, J. M. Wu, F. Zhang, Y. Zhou, Y. Zhang, Z. L. Wang, *ACS Nano* **2012**, *6*, 6984.
[8] D. Zhang, Y. Wang, Y. Yang, *Small* **2019**, *15*, 1805241.
[9] H. Ryu, S.-W. Kim, *Small* **2021**, *17*, 1903469.
[10] S. Anbalagan, K. Manojkumar, M. Muthuramalingam, S. Hajra, S. Panda, R. Sahu, H. Joon Kim, A. Sundaramoorthy, N. Nithyavathy, V. Vivekananthan, *Chem. Eng. J.* **2024**, *497*, 154740.

[11] Y. Fu, Y. Nie, Y. Zhao, P. Wang, L. Xing, Y. Zhang, X. Xue, *ACS Appl. Mater. Interfaces* **2015**, *7*, 10482.
[12] R. A. Shaukat, Q. M. Saqib, J. Kim, H. Song, M. U. Khan, M. Y. Chougale, J. Bae, M. J. Choi, *Nano Energy* **2022**, *96*, 107128.
[13] M. U. Khan, Y. Abbas, M. Rezeq, A. Alazzam, B. Mohammad, *Adv. Funct. Mater.* **2024**, *34*, 2305869.
[14] G. Sui, X. Shan, C. Zhou, H. Li, T. Cheng, *Nano Energy* **2024**, *130*, 110071.
[15] T.-W. Sun, M. Venkatesan, Y.-C. Hsu, J. Chandrasekar, W.-C. Chen, J.-S. Bénas, C.-J. Cho, J.-H. Lin, F.-C. Liang, A. Y. Rwei, C.-C. Kuo, *Nano Energy* **2025**, *133*, 110416.
[16] S. Shankhdhar, D. Arora, H. Rahman, R. Kumar, B. Ranjan, K. Kaushlendra, D. Kaur, *Nano Energy* **2025**, *133*, 110441.
[17] T. Das, S. Tripathy, A. Kumar, M. Kar, *Nano Energy* **2025**, *136*, 110752.
[18] T. Das, M. Kumar Yadav, A. Dev, M. Kar, *Chem. Eng. J.* **2024**, *496*, 153926.
[19] A. Khorsand Zak, S. T. Yazdi, M. E. Abrishami, A. M. Hashim, *J. Aust. Ceram. Soc.* **2024**, *60*, 723.
[20] R. F. Sagade Muktar Ahmed, S. B. Mohan, S. Madanahalli Ankanathappa, M. Shivanna, P. Viswanathan, H. C. S. Manjunatha, Y. S. Vidya, A. Chandrasekhar, K. Sannathammegowda, *ACS Appl. Electron. Mater.* **2023**, *5*, 5885.
[21] M. A. Farzin, S. M. Naghib, N. Rabiee, *ACS Biomater. Sci. Eng.* **2024**, *10*, 1262.
[22] B. Khan, Z. Riaz, *Mater. Sci. Eng., R* **2024**, *159*, 100804.
[23] H. Wei, H. Wang, Y. Xia, D. Cui, Y. Shi, M. Dong, C. Liu, T. Ding, J. Zhang, Y. Ma, N. Wang, Z. Wang, Y. Sun, R. Wei, Z. Guo, *J. Mater. Chem. C* **2018**, *6*, 12446.
[24] V. S. Kavarthapu, M. V. Paranjape, P. Manchi, A. Kurakula, J. K. Lee, S. A. Graham, J. S. Yu, *Small* **2024**, *20*, 2403218.
[25] Y. Yan, Y. Qiao, L. Wang, L. Jin, M. Zhang, Z. Li, M. Zhao, D. Zhang, *J. Mater. Sci. Technol.* **2024**, *221*, 25.
[26] Z. Cai, L. Li, J. Ren, L. Qiu, H. Lin, H. Peng, *J. Mater. Chem. A* **2013**, *1*, 258.
[27] Z. Yang, Y. Xu, T. Wang, Y. Huan, *J. Mater. Sci.* **2024**, *60*, 2407.
[28] S. Mondal, S. Maiti, T. Paul, S. Poddar, B. K. Das, K. K. Chattopadhyay, *ACS Appl. Mater. Interfaces* **2024**, *16*, 9231.
[29] Z. Zheng, X. Wang, G. Hang, J. Duan, J. Zhang, W. Zhang, Z. Liu, *Renewable Sustainable Energy Rev.* **2024**, *193*, 114285.
[30] U. Rajak, S. Molla, F. Khatun, N. Baugh, S. Banerjee, B. Bagchi, P. Thakur, *J. Mater. Sci. Mater. Electron.* **2024**, *35*, 1089.
[31] J. Peng, I. Witting, N. Geisendorfer, M. Wang, M. Chang, A. Jakus, C. Kenel, X. Yan, R. Shah, G. J. Snyder, M. Grayson, *Nat. Commun.* **2019**, *10*, 5590.
[32] M. Fahad, A. Waqar, B. Kim, *J. Alloys Compd.* **2024**, *985*, 174033.
[33] V. Lebedev, K. Lebedeva, A. Cherkashina, A. Voronkin, V. Kopach, S. Petrushenko, A. Fedonenko, N. Klochko, *Discov. Civ. Eng.* **2024**, *1*, 20.
[34] Y. Li, Z. Sun, M. Huang, L. Sun, H. Liu, C. Lee, *Adv. Energy Sustainability Res.* **2024**, *5*, 2400116.
[35] S. Hadidi, A. Hassanzadeh, *Int. J. Electron. Commun.* **2024**, *177*, 155197.
[36] F. Di Persio, M. Blecua, A. C. Chaine, T. Daue, C. Mateo-Mateo, I. Ezpeleta, P. Pötschke, B. Krause, E. Inci, J. Pionteck, T. Punkari, J. Keskinen, M. Mäntysalo, A. Melo, D. Esteves, *J. Clean. Prod.* **2024**, *435*, 140525.
[37] Q. Bai, T. Zhou, C. Gan, Q. Wang, X. Zheng, K.-X. Wei, *Energy Convers. Manage.* **2024**, *300*, 117971.
[38] Z. Peng, J. Li, H. Hao, *Eng. Struct.* **2023**, *293*, 116705.
[39] X. Hu, Y. Chen, X. Wang, K. Jia, H. Zhang, Y. Wang, H. Chu, X. Zhong, M. Lin, P. Chen, L. Qiu, H. Peng, S. He, *Adv. Funct. Mater.* **2024**, *34*, 2312897.
[40] S. S. Raj, D. Davis, P. Viswanathan, A. Chandrasekhar, *Macromol. Mater. Eng.* **2022**, *307*, 2200247.
[41] S. A. Basith, G. Khandelwal, D. M. Mulvihill, A. Chandrasekhar, *Adv. Funct. Mater.* **2024**, *34*, 2408708.
[42] A. R. Khan, R. Goel, A. Gupta, H. Tripathi, N. Kumar, S. Bhardwaj, S. Kumar, G. Kumar, P. Sharma, S. Kumar, *J. Mater. Sci. Mater. Electron.* **2024**, *35*, 1383.
[43] H. Wang, J. Tang, J. Liu, H. He, W. Wang, X. Li, K. Bi, *Ceram. Int.* **2024**, *50*, 46522.
[44] N. R. Alluri, A. Chandrasekhar, V. Vivekananthan, Y. Purusothaman, S. Selvarajan, J. H. Jeong, S.-J. Kim, *ACS Sustainable Chem. Eng.* **2017**, *5*, 4730.
[45] V. Vivekananthan, A. Chandrasekhar, N. R. Alluri, Y. Purusothaman, W. Joong Kim, C.-N. Kang, S.-J. Kim, *Mater. Lett.* **2019**, *249*, 73.
[46] V. Vivekananthan, N. R. Alluri, A. Chandrasekhar, Y. Purusothaman, A. Gupta, S.-J. Kim, *J. Mater. Chem. C* **2019**, *7*, 7563.
[47] A. Madani, M. Alghamdi, B. Alamri, S. Althobaiti, *Opt. Mater.* **2023**, *137*, 113480.
[48] S. Tangjuank, T. Tunkasiri, *Appl. Phys. Lett.* **2007**, *90*, 72908.
[49] T. Badapanda, V. Senthil, S. Panigrahi, S. Anwar, *J. Electroceram.* **2013**, *31*, 55.
[50] M. V. Paranjape, S. A. Graham, P. Manchi, A. Kurakula, J. S. Yu, *Small* **2023**, *19*, 2300535.
[51] M. V. Paranjape, S. A. Graham, P. Manchi, A. Kurakula, J. S. Yu, *J. Mater. Sci. Technol.* **2024**, *176*, 145.
[52] Q. Chen, Y. Cao, Y. Lu, W. Akram, S. Ren, L. Niu, Z. Sun, J. Fang, *ACS Appl. Mater. Interfaces* **2024**, *16*, 6239.